

# Kinematic dynamo action in a helical pipe

By L. ZABIELSKI<sup>1</sup> AND A. J. MESTEL<sup>2</sup>

<sup>1</sup>Mathematics Department, Warsaw University of Technology, 00-661 Warszawa, Poland

<sup>2</sup>Mathematics Department, Imperial College, 180 Queen's Gate, London SW7 2BZ, UK

(Received 9 September 2003 and in revised form 10 February 2005)

Steady incompressible laminar flow of an electrically conducting fluid down a helically symmetric pipe is investigated with regard to possible dynamo action. Both the fluid motion and the magnetic field are assumed to be helically symmetric, with the same pitch. Such a velocity field can be represented by its down-pipe component,  $v$ , and a streamfunction  $\Psi$  defining the secondary cross-pipe flow.

The helical geometry automatically links the cross-pipe and down-pipe field components and permits laminar dynamo action. It is found that the relatively weak secondary motion, which is always present in real pipe flows, has an inhibitory effect on the magnetic field growth and frequently suppresses dynamo action completely. In such a case for large magnetic Reynolds number ( $R_m \rightarrow \infty$ ) the asymptotic structure of the neutral mode is analysed using a streamline integral approach.

Kinematic velocity fields, without the cross-pipe flow ( $\Psi = 0$ ), usually generate a dynamo even for perfectly conducting walls. For large  $R_m$  the growing modes are shown to have a two-layer structure with rapid tangential variation.

For appropriate pipe geometry, steady pressure-driven pipe flow is found to drive a dynamo for moderate values ( $\sim 1000$ ) of the magnetic Reynolds number.

---

## 1. Introduction

The ability of motion of a conducting fluid to generate and sustain a magnetic field is important in astrophysical and geophysical contexts. On such length scales, not only is the motion likely to have a complex turbulent structure, but also the magnetic Reynolds number,  $R_m$ , is very high. Such dynamos typically rely on a turbulent ‘ $\alpha$ -effect,’ wherein averages over small-scale fluctuations arguably lead to an extra mean field term in the driving equations (e.g. Roberts & Soward 1992).

Despite a number of ‘anti-dynamo theorems,’ which require a minimum degree of flow complexity for dynamos to function, some flows with fairly simple structure are known to drive a dynamo, such as the Roberts (1972) and Ponomarenko (1973) flows. These dynamos are kinematic, in that the flow is prescribed rather than found dynamically. Simple models with a physically realizable flow field, and which extend into saturated states when the magnetic field reacts back on the driving flow, are much rarer. Usually another process is required to drive a sufficiently complex flow field, such as convection e.g. Matthews (1999), Kim, Hughes & Soward (1999).

This paper analyses a class of problems in which steady incompressible laminar flow of a Newtonian fluid down a pipe can drive a dynamo on laboratory length scales, with a pressure difference the only driving mechanism. Such dynamo action is of importance for liquid-metal pipe flows, which have been proposed as coolants for

nuclear reactors (Plunian, Marty & Alemany 1999), and in which the flow braking associated with dynamo action would present an operational hazard.

It is well-known that helical streamlines are advantageous for dynamos, and successful attempts to build laboratory dynamos encourage such flow structures (see the papers in the special issue Rädler & Cēbers 2002). Loosely speaking, the flows in the Karlsruhe and Riga dynamo experiments resemble respectively the Roberts and Ponomarenko velocity fields. Although in principle this paper has direct applicability to these experiments there are two difficulties in such a comparison. Firstly, the experiments are not exactly helically symmetric, and the geometry of this paper would require modification to allow, for example, for the return flow of metal. Secondly, this paper analyses a laminar dynamo, whereas due to the low magnetic Prandtl number of metals, any dynamo would almost certainly be turbulent. In this paper we do not consider the structure of turbulent helical pipe flow. This may be more of an issue in the future when nonlinear field equilibration is considered. It is found that the critical values of  $R_m$  in both the Riga and Karlsruhe dynamos are well predicted by laminar models, but the agreement is poor between the measured field values and those predicted by laminar theory (Fauve 2004).

In this paper the geometry is assumed to be helically symmetric in the precise sense described by Landman (1990), Childress, Landman & Strauss (1989), Dritschel (1991) and Zabielski & Mestel (1998*a*), and summarized in §1. The Navier–Stokes equations are invariant to this symmetry, and were solved for steady and unsteady pressure gradients in Zabielski & Mestel (1998*a*) and Zabielski & Mestel (1998*b*). In this paper the temporal behaviour of magnetic fields with the same helical symmetry will be investigated. Crucially, the equations for the down-pipe and cross-pipe magnetic field components are geometrically linked, without the need to resort to turbulence to provide an ‘ $\alpha$ -effect.’ While there may be other magnetic instabilities driven by helically symmetric flows which are not themselves helically symmetric, experience with the Ponomarenko (1973) dynamo suggests that modes with the same symmetry are close to those with the fastest growing instability (Gailitis & Freiberg 1977).

It is worth noting that subject to these assumptions a pressure-driven pipe flow which gives rise to a kinematic dynamo necessarily drives a fully nonlinear dynamo also. For were the driving flow to be quenched by the Lorentz force, and the field to die away, then the hydrodynamic pipe flow would once more be established on a viscous time scale and the dynamo process would repeat. This argument relies on the uniqueness of the steady driving flow, as found in Zabielski & Mestel (1998*a*). It would not necessarily be the case for flows with more than one solution e.g. Brummell, Cattaneo & Tobias 1998.

The earliest study of kinematic helical dynamos was by Lortz (1968), and later Benton (1979*a, b*) and Eltayeb & Loper (1988). The simple, solid body motion of the Ponomarenko (1973) dynamo was extended by Ruzmaikin, Sokoloff & Shukurov (1988) to any kinematic flow field dependent only on cylindrical radius. Gilbert (1988) demonstrated that the ‘fast’ dynamo action was a result of the velocity discontinuity. Taylor–Couette flow between two cylinders can also drive a dynamo (Dobler, Frick & Stepanov 2003; Willis & Barenghi 2002). A weakly nonlinear analysis for Taylor–Couette flow was provided by Bassom & Gilbert (1997). The physically realizable flow fields have a simple geometry, and rely on boundary motion to provide a sufficiently complex flow field. In this paper the boundary is fixed and the necessary helical motion is driven by the pipe shape. In principle, this dynamo could be driven by gravity in a sufficiently tall, helical pipe.

The structure of this paper is as follows: In §2 the helically symmetric problem is formulated and different electrical boundary conditions are discussed. In §3, a pipe of

square cross-section with perfectly conducting walls is investigated. These can obstruct dynamo action, in that the generated flux is restrained within the fluid domain wherein it is wound round by the cross-pipe flow and dissipated. This tendency is illustrated in §3.1 by an analysis of the asymptotic structure of the neutral mode as the magnetic Reynolds number,  $R_m \rightarrow \infty$  using a Prandtl–Batchelor streamline integral approach. In §3.2, the secondary flow is artificially repressed and dynamo action is found. The growing field exhibits a spatially quasi-periodic structure as  $R_m \rightarrow \infty$  on a tangential length scale  $R_m^{-1/3}$ , a normal length scale  $R_m^{-2/9}$  and with a growth rate of  $O(R_m^{-1/3})$ . It is shown that normal to the surface the field has a two-layer structure, with a lower layer of thickness  $R_m^{-1/3}$  required to match with the boundary conditions, which are otherwise passive.

In §4, the external medium is assumed to have the same conductivity as the fluid, as was the case in the Riga dynamo. The simplest case of solid body motion inside a cylinder was considered by Ponomarenko (1973) and Gilbert (1988), and a more general case in Gailitis & Freiberg (1980). In §4.1 this problem is reformulated using helical coordinates, with identical results. The effect of smoothing out the velocity discontinuity, which is primarily responsible for the fast dynamo action, is considered. Finally, in §4.2, laminar pressure-driven pipe in a rectangular pipe is considered. A dynamo is found in this geometry at a value  $R_m \sim 1000$ . This is the first steady laminar pressure-driven dynamo to be found. Its nonlinear evolution is currently under investigation and will be presented in a future work. Two factors are vital to the dynamo mechanism: firstly the ‘geometrical  $\alpha$ -effect’ or ‘torsion effect’ which is inherent to helical symmetry, and secondly the shear of the down-pipe flow. A third effect, the stretching of the field along the separation line of the cross-pipe flow, is important but frequently opposes the dynamo.

## 2. Mathematical formulation

In terms of cylindrical polar coordinates  $(r, \theta, z)$ , a scalar function is helically symmetric if it depends only on  $r$  and  $\phi = \theta + \varepsilon z$ , where  $\varepsilon$  is a constant. To be single-valued, the function must also be  $2\pi$ -periodic in  $\phi$ . Thus it is constant on helices with the same pitch,  $2\pi/\varepsilon$ . The symmetry direction is given by the vector

$$\mathbf{H} = \frac{\mathbf{e}_z - \varepsilon r \mathbf{e}_\theta}{h^2} \quad \text{where} \quad h = (1 + \varepsilon^2 r^2)^{1/2} \quad (2.1)$$

and  $\mathbf{e}_\theta$  and  $\mathbf{e}_z$  are the unit vectors in the  $\theta$ - and  $z$ -directions. Thus a scalar field  $f$  is helically symmetric if  $\mathbf{H} \cdot \nabla f = 0$ . The vector  $\mathbf{H}$  is a non-unit Beltrami field

$$\nabla \wedge \mathbf{H} = -\frac{2\varepsilon}{h^2} \mathbf{H}, \quad |h\mathbf{H}| = 1. \quad (2.2)$$

Helical symmetry spans the gulf between two-dimensionality ( $\varepsilon = 0$ ) and axisymmetry ( $\varepsilon \rightarrow \infty$ ). A detailed description of helical symmetry is given in Zabielski & Mestel (1998a).

As well as the helical parameter  $\varepsilon$ , which essentially measures the pipe torsion, the pipe dimensions determine its curvature. The pipe is assumed to have a rectangular cross-section in the poloidal plane  $\theta = 0$ , and occupies  $(b - a) < r < (b + a)$ , and  $0 < \phi < \phi_0$ . The geometry is defined by the dimensionless parameters  $\varepsilon b$ ,  $a/(bh_b)$  and  $\phi_0$  where  $h_b = \sqrt{1 + \varepsilon^2 b^2}$ . Helical effects depend on the torsion of the pipe centreline, and increase as the parameter  $2\varepsilon b/h_b^2$  increases. This is maximal at  $\varepsilon b = 1$ , and computations have concentrated on this case. It is found that the critical magnetic Reynolds number for dynamo action increases as the helicity effects decrease.

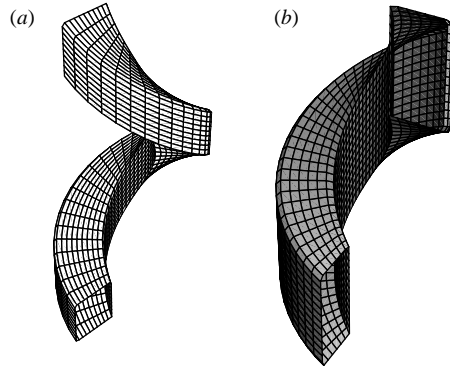


FIGURE 1. (a) Square and (b) ‘tall’ helical pipes, for  $\varepsilon = 1$ ,  $b = 2$ ,  $a = 0.5$ ,  $\phi_0 = 1, 2\pi/3$ .

In the numerical simulations the values used are  $a = 0.5$ ,  $b = 1$ ,  $\varepsilon = 1$  and the two cases  $\phi_0 = 1, 2\pi/3$ . These cases are denoted respectively the ‘square pipe’ and ‘tall pipe’. It will be found that dynamo action occurs only for the tall pipe, which is drawn in figure 1. The fluid domain is denoted by  $V$ , its exterior by  $\hat{V}$  and its bounding surface by  $S$ .

### 2.1. Fluid flow

An incompressible helically symmetric velocity field can be represented as

$$\mathbf{u} = \mathbf{H} \wedge \nabla \Psi + v \mathbf{H}. \quad (2.3)$$

The corresponding vorticity  $\boldsymbol{\omega} = \nabla \wedge \mathbf{u}$  then takes the form

$$\boldsymbol{\omega} = \mathbf{H} \wedge \nabla(-v) + \xi \mathbf{H}, \quad (2.4)$$

where

$$\mathcal{L}\Psi = \xi + \frac{2\varepsilon}{h^2}v, \quad (2.5)$$

and the elliptic operator  $\mathcal{L}$  is defined by

$$\mathcal{L} = \frac{h^2}{r} \frac{\partial}{\partial r} \left( \frac{r}{h^2} \frac{\partial}{\partial r} \right) + \frac{h^2}{r^2} \frac{\partial^2}{\partial \phi^2}. \quad (2.6)$$

The  $\mathbf{H}$ -component of the Navier–Stokes equations is then (Zabielski & Mestel 1998a)

$$\frac{\partial v}{\partial t} + \frac{1}{r} J(\Psi, v) = G + F_1 + \nu \left( \mathcal{L}v + \frac{2\varepsilon}{h^2} \xi \right) \quad (2.7)$$

where  $G$  is the driving down-pipe pressure gradient per unit mass,  $F_1$  a suitable component of the Lorentz force defined in (2.18) and  $\nu$  is the kinematic viscosity. The Jacobian  $J$  is defined by

$$\frac{1}{r} J(f, g) \equiv \frac{1}{r} \left( \frac{\partial f}{\partial r} \frac{\partial g}{\partial \phi} - \frac{\partial f}{\partial \phi} \frac{\partial g}{\partial r} \right) = \mathbf{H} \cdot (\nabla f \wedge \nabla g). \quad (2.8)$$

The  $\mathbf{H}$ -component of the vorticity equation takes the form

$$\frac{\partial \xi}{\partial t} - \frac{2\varepsilon}{h^2} \frac{1}{r} J(\Psi, v) + \frac{1}{r} J(\Psi, \xi) + \frac{2\varepsilon^2}{h^2} \left( \xi \frac{\partial \Psi}{\partial \phi} + v \frac{\partial v}{\partial \phi} \right) = F_2 + \nu \left( \mathcal{L}\xi - \frac{2\varepsilon}{h^2} \left( \mathcal{L}v + \frac{2\varepsilon}{h^2} \xi \right) \right) \quad (2.9)$$

where  $F_2$  is the  $\mathbf{H}$ -component of the curl of the Lorentz force as in (2.19). The system of equations (2.7), (2.9) and (2.5) together with a non-slip condition on the pipe boundary determines a general helically symmetric pipe flow. In this paper only steady pressure gradients are considered so that for a fixed geometry, flows are determined by a single parameter, the Reynolds number

$$R_e = h_b \frac{G(2a)^3}{\nu^2}. \quad (2.10)$$

For consistency with Zabielski & Mestel (1998a) this definition of  $R_e$  will be used, but it would also be possible to scale with the flow rate, or maximum velocity, giving a numerical value typically fifty times smaller. For the kinematic problem only the structure of the velocity field is important. The magnetic Reynolds number,  $R_m$ , is defined based on the maximum of the down-pipe velocity,  $v_m$ ,

$$\eta^{-1} \equiv R_m = \frac{2av_m}{\eta^*}, \quad (2.11)$$

where  $\eta^*$  is the magnetic diffusivity of the fluid. From now on,  $\eta$  may be used as a shorthand for  $R_m^{-1}$ . Clearly, defining  $R_m$  with respect to the mean flow rate, say, would lead to lower numerical values, by a factor of about 4.

## 2.2. The magnetic field

The fluid region is assumed to have constant electrical conductivity  $\sigma$  and magnetic permeability  $\mu$ , so that its magnetic diffusivity is  $\eta^* = 1/(\mu\sigma)$ . The helically symmetric solenoidal ( $\nabla \cdot \mathbf{B} = 0$ ) magnetic field  $\mathbf{B}$  is expressed analogously to (2.3) as

$$\mathbf{B} = \mathbf{H} \wedge \nabla \chi + B\mathbf{H} \quad (2.12)$$

so that the current density  $\mathbf{j}$  follows from Ampère's law

$$\mu \mathbf{j} = \nabla \wedge \mathbf{B} = \mathbf{H} \wedge \nabla(-B) + \gamma \mathbf{H} \quad \text{where} \quad \gamma = \mathcal{L} \chi - \frac{2\varepsilon}{h^2} B. \quad (2.13)$$

The electric field  $\mathbf{E}$  is related to  $\mathbf{j}$  by Ohm's law

$$\mathbf{j} = \sigma(\mathbf{E} + \mathbf{u} \wedge \mathbf{B}), \quad (2.14)$$

which with Faraday's law  $\nabla \wedge \mathbf{E} = -\partial \mathbf{B} / \partial t$  implies the induction equation

$$\frac{\partial \mathbf{B}}{\partial t} = \nabla \wedge (\mathbf{u} \wedge \mathbf{B}) - \nabla \wedge (\eta \nabla \wedge \mathbf{B}). \quad (2.15)$$

Only cases with piecewise constant  $\eta$  are presented here, so that (2.15) is similar in form to the vorticity equation. Substituting (2.3) and (2.12) into (2.15) one can then derive the following two scalar equations:

$$\frac{\partial \chi}{\partial t} + \frac{1}{r} J(\Psi, \chi) = \eta \left( \mathcal{L} \chi - \frac{2\varepsilon}{h^2} B \right) \equiv \eta \gamma \quad (2.16)$$

and

$$\frac{\partial B}{\partial t} - \frac{2\varepsilon}{h^2} \frac{\partial \chi}{\partial t} + \frac{h^2}{r} \left( J \left( \frac{v}{h^2}, \chi \right) + J \left( \Psi, \frac{B}{h^2} \right) \right) = \eta \mathcal{L} B. \quad (2.17)$$

A similar set of equations was derived by Benton (1979a). Equation (2.16) is essentially the  $\mathbf{H}$ -component of Ohm's law (2.14), where it is assumed that there is no externally imposed electric field in the  $\mathbf{H}$ -direction. Equation (2.17) is the  $\mathbf{H}$ -component of the induction equation (2.15).

It is readily seen that the equations for  $B$  and  $\chi$ , which are respectively the helical analogues of toroidal and poloidal fields, are linked. In (2.17) the third term involves the advection of the cross-pipe  $\chi$ -lines by the down-pipe velocity  $v$  in a manner akin to differential rotation in an astrophysical context. The second term also provides a geometrical linkage with  $\chi$ , but this effect is usually weaker. In (2.16), the linkage with  $B$  is a consequence of the Beltrami property (2.2) of the helical symmetry direction  $\mathbf{H}$  that captures genuinely three-dimensional behaviour. It should be noted that this term is proportional to  $\eta$ , so that any dynamo is expected to be ‘diffusive’ in nature. Since Cowling’s theorem prohibits dynamo action in the axisymmetric ( $\varepsilon \rightarrow \infty$ ) and the two-dimensional ( $\varepsilon = 0$ ) cases, for a successful dynamo the torsion terms of non-planar geometry must play a significant rôle.

Calculation leads to the Lorentz force,  $\mathbf{j} \wedge \mathbf{B}$  and its curl. In the Navier–Stokes equations (2.7) and (2.9),

$$F_1 = h^2 \mathbf{H} \cdot (\mathbf{j} \wedge \mathbf{B}) = -\frac{1}{\mu r} J(B, \chi), \quad (2.18)$$

$$F_2 = h^2 \mathbf{H} \cdot [\nabla \wedge (\mathbf{j} \wedge \mathbf{B})] = \frac{1}{\mu} \left( \frac{2\varepsilon}{h^2} \frac{1}{r} J(B, \chi) - \frac{h^2}{r} J\left(\frac{\gamma}{h^2}, \chi\right) + \frac{2\varepsilon^2}{h^2} \mathbf{B} \frac{\partial B}{\partial \phi} \right). \quad (2.19)$$

### 2.3. Boundary conditions

In this paper, the fluid boundary,  $S$ , is rigid and stationary so that  $\mathbf{u} = 0$  in  $S$ . To complete the problem description, electromagnetic conditions must be specified on  $S$  where  $\sigma$  and  $\mu$  may be discontinuous. The effect of a tangential slip velocity is also considered below as in the Ponomarenko case. If square brackets are used to denote jumps across an interface with normal  $\mathbf{n}$ , the standard continuity conditions are

$$[\mathbf{B} \cdot \mathbf{n}] = 0, \quad [\mathbf{n} \wedge \mathbf{B} / \mu] = \mathbf{j}_s \quad \text{and} \quad [\mathbf{n} \wedge \mathbf{E}] = 0, \quad (2.20)$$

where  $\mathbf{j}_s$  is a surface current, which exists only when one medium is a perfect conductor. Assuming this is not the case, and that the permeability,  $\mu$ , is continuous, the first two conditions in (2.20) imply continuity of  $\mathbf{B}$ , that is, of  $\chi$ ,  $\mathbf{n} \cdot \nabla \chi$  and  $B$ . Now from (2.12), (2.13) and (2.14),

$$\mathbf{n} \wedge \mathbf{E} = \mathbf{n} \wedge (\mathbf{j} / \sigma - \mathbf{u} \wedge \mathbf{B}) \quad (2.21)$$

$$= -\eta(\mathbf{n} \cdot \nabla B) \mathbf{H} + \eta \gamma \mathbf{n} \wedge \mathbf{H} - (\mathbf{B} \cdot \mathbf{n}) \mathbf{u}, \quad (2.22)$$

since  $\mathbf{u} \cdot \mathbf{n} = 0$  on  $S$  and  $\mathbf{H} \cdot \mathbf{n} = 0$  by the symmetry. Continuity of the tangential  $\mathbf{n} \wedge \mathbf{H}$ -component of (2.21) is dealt with by (2.16) and the continuity of  $\chi$ , but the  $\mathbf{H}$ -component provides a condition on  $\mathbf{n} \cdot \nabla B$ . Thus the boundary conditions in the general case are

$$[\chi] = 0, \quad [\mathbf{n} \cdot \nabla \chi] = 0, \quad [B] = 0, \quad [\eta \mathbf{n} \cdot \nabla B] = -(\mathbf{n} \cdot \mathbf{B}) [v]. \quad (2.23)$$

A discontinuity in  $\mathbf{n} \cdot \nabla B$  therefore results from a discontinuity either in the electrical property  $\eta$  or in the velocity field. Three particular limits of (2.23) will be considered, when the external conductivity is zero, infinite, or the same as in the fluid.

The smoothest boundary conditions occur when  $\eta$  is the same in  $V$  and  $\widehat{V}$ , so that the exterior is filled with solid material of the same conductivity as the fluid. Then if the flow obeys the no-slip condition,  $\chi$ ,  $B$  and their normal derivatives are continuous:

$$[\chi] = 0, \quad [\mathbf{n} \cdot \nabla \chi] = 0, \quad [B] = 0, \quad [\mathbf{n} \cdot \nabla B] = 0. \quad (2.24)$$

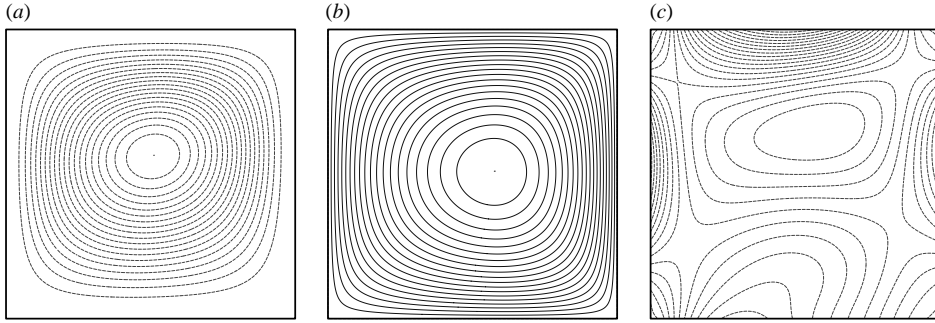


FIGURE 2. Velocity patterns at  $R_e = 10^3 h_b$  for the square pipe: (a) cross-pipe streamfunction  $\Psi$ ; (b) down-pipe velocity  $v$ ; (c) down-pipe vorticity  $\xi$ .  $\max(\Psi) = 5 \times 10^{-4}$ ,  $\max(v) = 0.024$ . The inside of the pipe is on the left.

If, as in the Ponomarenko dynamo (§4.1),  $[v] \neq 0$ , then a discontinuity in the normal derivative of  $B$  is needed.

When the external conductivity is zero,  $j = 0$  in  $\hat{V}$ , which, from (2.13), requires that

$$\mathcal{L}\chi = \frac{2\varepsilon}{h^2} B_0 \quad B_0 = \text{const.} \quad \text{in } \hat{V} \quad (\text{insulating exterior}) \quad (2.25)$$

and  $B$ ,  $\chi$  and  $\mathbf{n} \cdot \nabla \chi$  are continuous across  $S$ . If conditions at infinity are such that no net current flows in the  $\mathbf{H}$ -direction then  $B_0 = 0$ .

A perfectly conducting medium can support no electric field, so that the tangential electric field in the fluid must vanish by (2.20). Further, by Faraday's law, no growing  $\mathbf{B}$  can exist in  $\hat{V}$ . Thus the internal normal field  $\mathbf{B} \cdot \mathbf{n} = 0$ , so that  $\chi = 0$ , but the tangential field need not vanish owing to the possible surface current. Thus (2.21) requires  $\gamma = 0$  and  $\mathbf{n} \cdot \nabla B = 0$  on  $S$ . From (2.13) and (2.16),  $\gamma = 0$  if  $\chi = 0$  on the rigid boundary  $S$ . Thus the appropriate boundary conditions are

$$\chi = 0 \quad \text{and} \quad \mathbf{n} \cdot \nabla B = 0 \quad \text{on } S \quad (\text{perfectly conducting walls}). \quad (2.26)$$

The perfectly conducting walls keep the magnetic field trapped within  $V$ .

The above boundary conditions have assumed no variation in magnetic permeability,  $\mu$ , across  $S$ . One could also postulate a ferromagnetic boundary, for which  $\mu \rightarrow \infty$  in  $\hat{V}$ . Then, from (2.20), the tangential component of  $\mathbf{B}$  must vanish on the fluid boundary, so that

$$B = 0 \quad \text{and} \quad \mathbf{n} \cdot \nabla \chi = 0 \quad \text{on } S \quad (\text{ferromagnetic walls}). \quad (2.27)$$

#### 2.4. Numerical simulations

The equations (2.16) and (2.17) with an appropriate version of (2.23)–(2.27) are solved numerically using finite differences. An implicit time-stepping method is used, second order in space and time, similar to that described in Zabielski & Mestel (1998*a, b*). For the kinematic problem, the Lorentz force terms  $F_1$  and  $F_2$  are neglected and the fully developed Navier–Stokes flow can be found independently, whereas for the dynamic problem (2.7) and (2.9) would have to be solved simultaneously. The flow structure depends on  $R_e$ , and two cases are shown in figures 2 and 3. In each case the inside of the helix is on the left and the pipe spirals clockwise as in figure 1. Panel (a) shows the contours in the  $(r, \phi)$ -plane of the secondary flow streamfunction,  $\Psi$ , (b) gives the contours of the down-pipe velocity  $v$ , and the down-pipe vorticity component  $\xi$  is shown in (c). The secondary flow is always present, although its

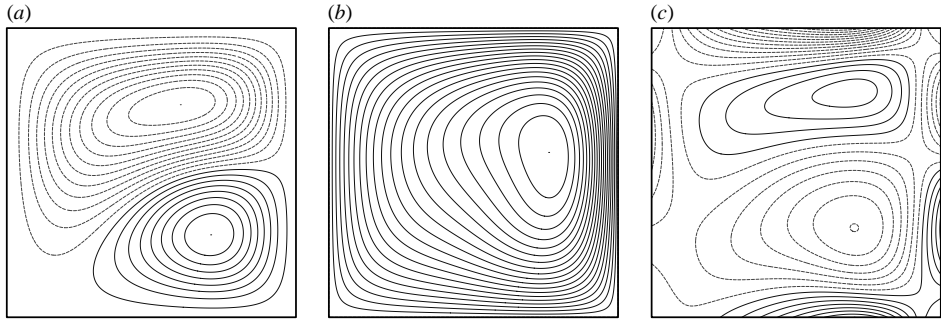


FIGURE 3. Velocity patterns at  $R_e = 20^3 h_b$  for square pipe: (a)  $\Psi$ ; (b)  $v$ ; (c)  $\xi$ .  $\max(\Psi) = 4 \times 10^{-4}$ ,  $\max(v) = 0.02$ . At this  $R_e$  the secondary flow has a separation point.

magnitude is typically about 50 times smaller than the down-pipe component in the parameter ranges considered here. For low  $R_e$  it takes the form of a single anticlockwise gyre. As  $R_e$  increases, a second clockwise gyre appears at the bottom of the figure, with associated separation and attachment points. As  $R_e \rightarrow \infty$  the symmetrical configuration of Dean flow is approached (Zabielski & Mestel 1998a). This structure of the secondary flow is highly significant, as the stretching of magnetic field is strong near separation points of the secondary flow.

As the time evolution is followed an eigenvalue  $\lambda$  is identified such that

$$\mathbf{B} \sim \text{Re} [\mathbf{B}_0(r, \phi) \exp(\lambda t)] \quad \text{as } t \rightarrow \infty. \quad (2.28)$$

For an arbitrary initial state, a qualitative eigenfunction structure usually appears fairly quickly. However, considerable care is required to ensure that the grid size and time step are small enough to resolve the small, complex eigenvalue. The method used is not the most efficient for calculating eigenvalues, but was chosen with a view to future extension of the calculation into the dynamic regime when the field reacts back on the driving flow. Sometimes thin layer regions develop, but a grid size  $160 \times 160$  in the  $(r, \phi)$ -plane over the pipe cross-section proved adequate for the  $R_m$  range considered.

The eigenvalue  $\lambda$  is usually complex, and its real part typically becomes positive at a value of  $R_m$  in the range (100, 1000), if dynamo action occurs. It decays to zero algebraically as  $R_m \rightarrow \infty$ , so that the dynamo is 'slow'. The corresponding eigenfunctions exhibit a variety of structures, and depend upon the magnetic boundary conditions imposed.

### 3. Perfectly conducting walls

When the exterior is perfectly conducting, so that (2.26) is satisfied, the field is confined to the fluid region. It is therefore wound up very tightly by the secondary motion to a level where diffusion can act. Regions with high gradients are therefore anticipated for high  $R_m$ .

A further feature of this boundary condition follows from integrating Faraday's law over a pipe cross-section. As the tangential component of  $\mathbf{E}$  vanishes over the boundary, it follows that the integral of  $\partial \mathbf{B} / \partial t$  over the cross-section is zero. The total flux of  $\mathbf{B}$  along the pipe is thus constant, and hence the equations must have a neutral mode, for which  $\lambda = 0$ . If no dynamo action occurs, a general initial condition approaches this mode. If the velocity is zero, the neutral mode is just a potential field,

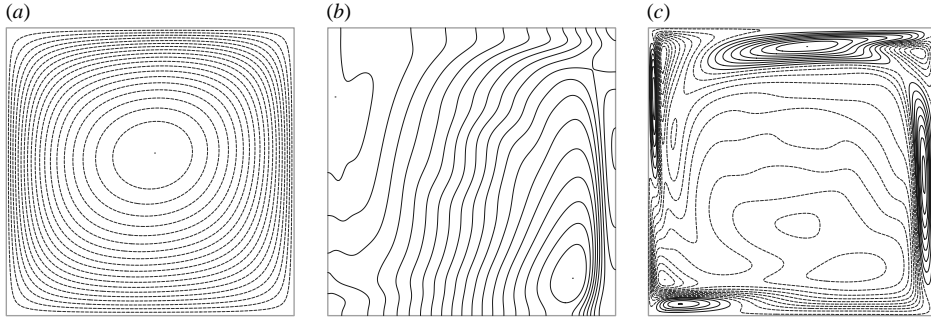


FIGURE 4. The neutral mode for  $R_m = 30^3$ ,  $Re = 10^3 h_b$  and square pipe: (a) cross-pipe field  $\chi$ ; (b) downpipe field  $B$ ; (c) downpipe current,  $\gamma$ .  $\max(\chi)/\max(B) = 0.019$ . The walls are perfectly conducting.

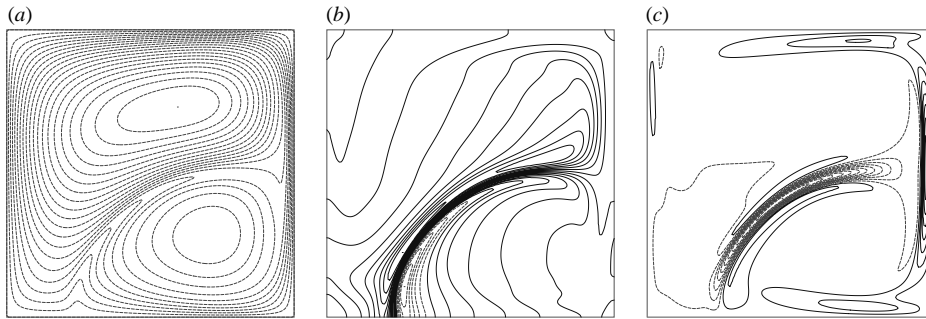


FIGURE 5. The neutral mode for square pipe with  $R_m = 30^3$ ,  $Re = 20^3 h_b$ : (a)  $\chi$ ; (b)  $B$ ; (c)  $\gamma$ .  $\max(\chi)/\max B = 0.011$ . The walls are perfectly conducting. Stretching occurs along the separatrix of  $\Psi$ .

$\mathbf{B} = \nabla f$  for some function  $f$ , satisfying (2.26). This neutral mode is a consequence of the perfectly conducting walls. As the kinematic problem is linear it does not interact with any of the other modes, although its spatial structure is found to be similar.

For the square pipe, with flow structures such as those of figures 2 and 3, no growth is found for any value of  $R_m$ , and the field decays towards the neutral mode. Typical examples are shown in figures 4 and 5 for a fairly high value of  $R_m$ . Comparison with figures 2 and 3 indicates a strong dependence of the field on the secondary motion as exhibited by the shape of the  $\Psi$  contours. There also appears to be an asymptotic structure as  $R_m \rightarrow \infty$  with a core and boundary layers. This asymptotic limit is considered below.

### 3.1. Neutral mode as $R_m \rightarrow \infty$ ; Prandtl–Batchelor analysis

In this section it is demonstrated how the asymptotic structure of the neutral mode at high  $R_m$  can, in principle, be derived from the driving velocity field using a streamline integral approach. This method is discussed in Childress & Gilbert (1995) but there are few geometries for which it can be used. There are strong similarities with steady hydrodynamic problems with closed streamlines. The analysis also holds for weakly growing or decaying modes with  $\lambda \sim \eta$ . In the fluid core, as  $\eta \rightarrow 0$  expand

$$\chi \sim \chi_0 + \eta\chi_1 + \dots \quad B \sim B_0 + \dots \quad \lambda \sim \eta\lambda_0 + \dots \quad (3.1)$$

so that in (2.16) and (2.17), at leading order,

$$J(\Psi, \chi_0) = 0, \\ J\left(\frac{v}{h^2}, \chi_0\right) + J\left(\Psi, \frac{B_0}{h^2}\right) = 0.$$

or

$$\chi_0 = \chi_0(\Psi), \quad \frac{B_0}{h^2} = f(\Psi) + \chi_0'(\Psi) \frac{v}{h^2}. \quad (3.2)$$

Thus in a manner akin to the Euler equations, the steady magnetic field is functionally related to the velocity streamfunction. As in Prandtl–Batchelor theory (Batchelor 1956), these functions are determined at high  $R_m$  by integrating the magnetic field equations (2.16), (2.17) over the helical path  $\Psi = \text{const}$ . Although the streamlines of the full flow are not closed because of the down-pipe motion, nevertheless the advective velocity terms  $J(\Psi, \cdot)$  still integrate to zero under helical symmetry around a  $\Psi$ -contour (cf. Childress *et al.* 1989). Thus the integrated effects of the small diffusive terms must balance and it can hence be shown that

$$0 = \oint_{\Psi} \left( \mathcal{L}\chi_0 - 2\varepsilon \frac{B_0}{h^2} \right) \frac{dl}{q}, \quad (3.3)$$

$$\oint_{\Psi} \frac{1}{r} J\left(\frac{v}{h^2}, \chi_1\right) \frac{dl}{q} = \oint_{\Psi} \frac{1}{h^2} \mathcal{L}B_0 \frac{dl}{q}, \quad (3.4)$$

with the secondary flow speed  $q = (1/h)|\nabla\Psi|$ , and  $dl$  denotes arclength in the  $(r, \phi)$ -plane. After some manipulation one finds that (3.3) and (3.4) imply that  $f(\Psi)$  and  $\chi_0(\Psi)$  must satisfy the ODEs

$$a_2\chi_0'' + a_1\chi_0' = 2\varepsilon a_0 f, \quad (3.5)$$

$$c_2 f'' + c_1 f' + c_0 f + b_3 \chi_0''' + b_2 \chi_0'' + b_1 \chi_0' = \oint_{\Psi} \frac{1}{r} J\left(\frac{v}{h^2}, \chi_1\right) \frac{dl}{q}, \quad (3.6)$$

with the coefficients

$$a_0 = \oint_{\Psi} \frac{dl}{q}, \quad a_1 = \oint_{\Psi} \xi \frac{dl}{q}, \quad a_2 = \oint_{\Psi} |\nabla\Psi|^2 \frac{dl}{q}, \\ b_1 = \oint_{\Psi} \frac{1}{h^2} \mathcal{L}v \frac{dl}{q}, \quad b_2 = \oint_{\Psi} \left( \frac{2}{h^2} \nabla v \cdot \nabla\Psi + \frac{v}{h^2} \mathcal{L}\Psi \right) \frac{dl}{q}, \quad b_3 = \oint_{\Psi} \frac{v}{h^2} |\nabla\Psi|^2 \frac{dl}{q}, \\ c_0 = \oint_{\Psi} \frac{4\varepsilon^2}{h^4} \frac{dl}{q}, \quad c_1 = \oint_{\Psi} \left( \mathcal{L}\Psi + \frac{4\varepsilon^2 r}{h^2} \frac{\partial\Psi}{\partial r} \right) \frac{dl}{q}, \quad c_2 = \oint_{\Psi} |\nabla\Psi|^2 \frac{dl}{q},$$

where all the  $a_i = a_i(\Psi)$ ,  $b_i = b_i(\Psi)$ ,  $c_i = c_i(\Psi)$  and are calculable from the known velocity field. To evaluate the term on the right-hand side of (3.6) it is necessary to evaluate (2.16) at  $O(\eta)$ , when

$$\frac{1}{r} J(\Psi, \chi_1) = \mathcal{L}\chi_0 - \frac{2\varepsilon}{h^2} B_0 - \lambda_0 \chi_0. \quad (3.7)$$

For the neutral mode  $\lambda_0 = 0$ . This determines  $\chi_1$  apart from an arbitrary function of  $\Psi$  which does not contribute to the integral in (3.6). The differential equations (3.5) and (3.6) hold in any closed  $\Psi$ -region, say  $0 < \Psi < \Psi_m$  where  $\Psi = \Psi_m$  at the stagnation point where  $\nabla\Psi = 0$ . The equations are singular at both the endpoints. Four boundary conditions are required to determine  $f$  and  $\chi_0$  if the eigenvalue  $\lambda_0$  is regarded as unknown.

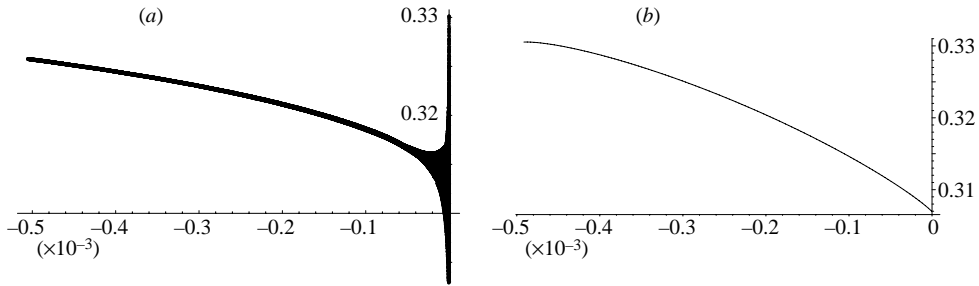


FIGURE 6. Neutral mode:  $B/h^2$  as a function of  $\Psi$  for  $v=0$  and  $\Psi$  as in figure 2. (a) Scatterplot of the steady solution to (2.16) and (2.17). (b) Solution of (3.6).

Writing  $p = \sqrt{2\sqrt{|\Psi - \Psi_m|}}$ , a local analysis about the point where  $\Psi = \Psi_m$  shows that

$$\chi'_0 = 0 \quad \text{and} \quad \frac{df}{dp} + \frac{1}{2}v \frac{d^3\chi_0}{dp^3} = 0 \quad \text{at} \quad \Psi = \Psi_m. \quad (3.8)$$

One condition on the wall  $\Psi = 0$  is straightforward to apply,

$$\chi_0(0) = 0. \quad (3.9)$$

The boundary condition (2.26) cannot be imposed subject to the constraint (3.2) and a boundary layer of thickness  $\eta^{1/3}$  is required. The final boundary condition derives from an integral over this wall layer. Writing  $x = \sqrt{\Psi}$  it takes the form

$$\alpha \frac{df}{dx} + \beta \frac{d\chi_0}{dx} + \gamma \frac{d^2\chi_0}{dx^2} + \delta f = 0 \quad \text{on} \quad \Psi = 0, \quad (3.10)$$

where  $\alpha$ ,  $\beta$ ,  $\gamma$  and  $\delta$  are known in terms of  $v$  and  $\Psi$ . In general  $f(\Psi)$  has a square-root singularity at  $\Psi = 0$ .

It is therefore possible in principle to determine the asymptotic form of the field by solving the ODEs (3.5), (3.6) with (3.7) subject to the conditions (3.8), (3.9) and (3.10). The coefficients are expressed as path integrals along known contours, unlike in similar hydrodynamic problems where the vorticity is constant on streamlines which must themselves be found as part of the solution. Although evaluation of the coefficients and boundary conditions is tedious, the resulting problem for  $\chi_0$  and  $f$  is linear, and homogeneous. As it has been shown that a neutral mode must exist with an amplitude determined by the down-pipe flux, it follows that the problem has an eigensolution, and one of the boundary conditions is redundant.

Note, however, that this structure applies only on a single set of nested streamlines. For a flow field such as figure 3 giving rise to figure 5, different functions  $f(\Psi)$  and  $\chi_0(\Psi)$  should be used in each separate gyre. These must be matched across an  $\eta^{1/3}$  layer about the stagnation streamline. The method is illustrated in figure 6 for the simple kinematic flow with a single  $\Psi$ -gyre as in figure 2 but with  $v=0$ . This latter condition ensures  $b_i = 0$ , and also that the inconvenient term on the right-hand side of (3.6) vanishes. In figure 6 the calculated values of  $B/h^2$  for  $R_m = 20^3$  are plotted against  $\Psi$  for the entire grid. Except near the wall, the data collapse onto a single curve, as expected. Also, shown in figure 6(b) is the function  $f(\Psi)$  obtained by solving (3.6). The resulting asymptotic form of  $f(\Psi)$  is consistent with the numerical results for  $R_m = 20^3$ , but there is still some quantitative disagreement for this value of  $R_m$ , with the ODE predicting a slightly sharper gradient. Overall, the entire approach, while of undoubted theoretical interest, appears overelaborate for quantifying the asymptotic

structure as  $R_m \rightarrow \infty$  of a neutral mode, which is readily obtained numerically for finite  $R_m$ . It would only be worthwhile should the fastest growing mode have  $\lambda \sim \eta$  as  $\eta \rightarrow 0$ , whereas usually  $\lambda \sim \eta^{1/3}$ .

Numerical calculations suggest that no helically symmetric dynamo occurs for pressure-driven flows down the square pipe  $a = 0.5$ ,  $b = 1$ ,  $\varepsilon = 1$ ,  $\phi_0 = 1$  for any values of  $R_e$  and  $R_m$ . Likewise, no growth was found if the exterior was insulating or of finite conductivity. The secondary flow in this geometry is too strong over the numerically accessible  $R_e$ -range, leading to 'flux expulsion' and quenching of the dynamo. By artificially reducing the size of this secondary flow, however, magnetic growth is obtained in the next section for flows which are kinematically admissible but do not correspond to the genuine pipe flow. For  $R_e = 10^3 h_b$ , the real flow has a secondary pipe component which is about ten times too large for dynamo action. Nevertheless, dynamo action in this geometry may theoretically be possible at extremely high Reynolds number. As  $R_e$  (or for small curvature a Dean number) approaches infinity, the ratio of the secondary to primary core velocities tends to zero for steady laminar flow, e.g. Zabielski & Mestel (1998a). Such flows would probably drive a kinematic dynamo, as the secondary flow will be negligible. Some numerical results bear this conjecture out, but the resolution of the viscous boundary layer is questionable and they are not presented here. In reality, these steady flows will certainly be unstable and so are of questionable practical relevance.

More importantly, a dynamo is found to occur with perfectly conducting walls for the genuine laminar flow in the tall pipe with  $\phi_0 = 2\pi/3$ . This case is described briefly in Zabielski & Mestel (2004). This geometry with finite external conductivity is investigated in §4.2.

### 3.2. Kinematic dynamo with no cross-pipe flow ( $\Psi = 0$ )

To demonstrate the obstructive nature of the cross-pipe flow as regards dynamo action, this section investigates the simpler flows with  $\Psi = 0$ . Equations (2.16) and (2.17) then take the form

$$\lambda \chi = \eta \left( \mathcal{L} \chi - \frac{2\varepsilon B}{h^2} \right), \quad (3.11)$$

$$\lambda \left( B - \frac{2\varepsilon \chi}{h^2} \right) = -\frac{h^2}{r} J \left( \frac{v}{h^2}, \chi \right) + \eta \mathcal{L} B. \quad (3.12)$$

The simplest flow field of this form is the solid body motion of the Ponomarenko dynamo (Ponomarenko 1973). Such a flow field in helical coordinates takes the form

$$\mathbf{u} = v_c h^2 \mathbf{H} = -v_c \varepsilon r \mathbf{e}_\theta + v_c \mathbf{e}_z, \quad v_c = \text{const.} \quad (3.13)$$

Putting  $v = v_c h^2$  in (3.11) and (3.12) it is clear that no velocity terms remain in the equations. The Ponomarenko dynamo requires an external region and is driven by the discontinuous flow field and the boundary conditions (2.23). In the case of perfectly conducting boundaries, however, the velocity (3.13) leads to

$$\frac{\partial \mathbf{B}}{\partial t} = \eta \nabla^2 \mathbf{B} \quad \implies \quad \frac{\partial \mathbf{j}}{\partial t} = \eta \nabla^2 \mathbf{j}. \quad (3.14)$$

Since the boundary conditions (2.26) require  $\mathbf{n} \wedge \mathbf{j} = 0$  on  $S$  it follows that

$$\frac{\partial}{\partial t} \int_V \frac{1}{2} |\mathbf{j}|^2 dV = -\eta \int_V |\nabla \wedge \mathbf{j}|^2 dV$$

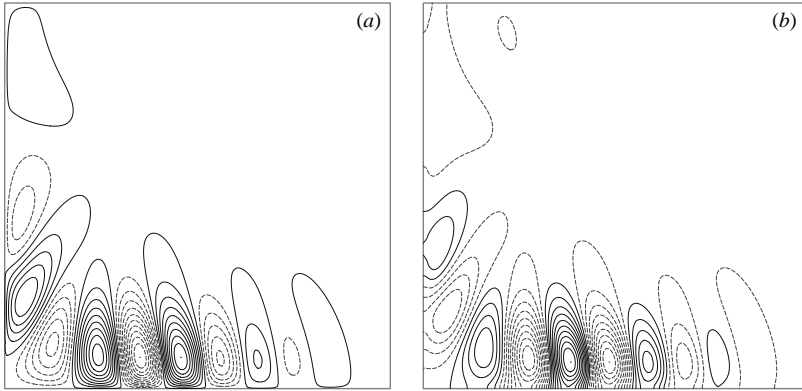


FIGURE 7. The magnetic field for  $R_m = 50^3$ , with  $\Psi = 0$  and  $v$  as in figure 3. A rapid tangentially varying structure emerges. (a)  $\chi$ , (b)  $B$ ;  $\max(\chi)/\max(B) = 3 \times 10^{-4}$ .

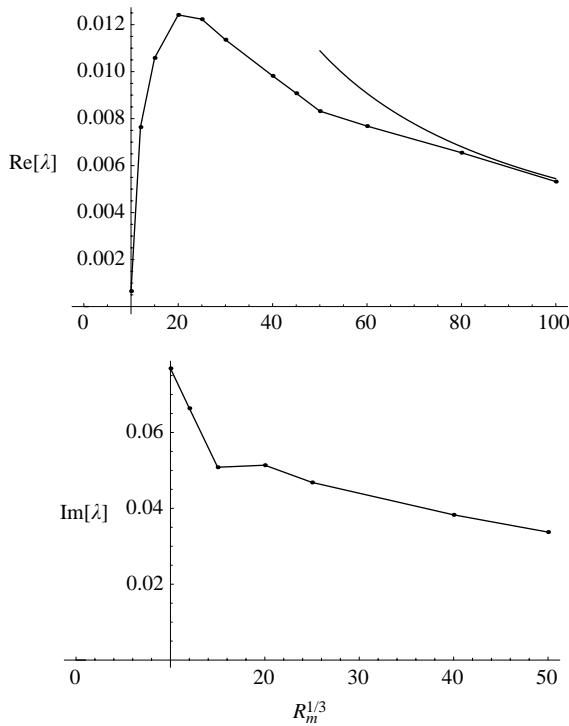


FIGURE 8. The real and imaginary parts of the dominant eigenvalue for  $\Psi = 0$  and  $v$  as in figure 3. Also shown is the asymptotic result  $\text{Re}[\lambda] \sim 0.545 R_m^{-1/3}$ .

and hence the current cannot grow in this case, as observed in Gailitis & Freiberg (1980). No such constraint holds if the linkage term  $J(v/h^2, \chi)$  does not vanish, and the velocity field of figure 3 is now considered, but with the cross-pipe component  $\Psi = 0$ . This kinematic flow is found to excite a dynamo, and in figure 7 the growing eigenfunction is drawn for a large value of  $R_m$ . As time evolves, the eigenfunction travels around the boundary for moderate  $R_m$ , but for higher values it appears, rather, to oscillate along the lower wall. Figure 8 depicts the behaviour of the real

and imaginary parts of the growth rate  $\lambda$  with  $R_m$ . These are of similar order, and it seems that  $\lambda \sim R_m^{-1/3}$  as  $R_m \rightarrow \infty$ . It becomes harder to resolve  $\text{Im}[\lambda]$  as  $R_m$  increases, as the data have to be collected over a longer time. The imaginary part exhibits a slight kink near the maximum of the real part.

The numerics suggest that as  $R_m$  increases the preferred mode develops rapid variation tangential to the boundary. In terms of local coordinates  $(n, s)$  normal and tangential to the boundary, one might therefore seek a solution to (3.11) and (3.12) of the form  $\chi \sim e^{\lambda t + ik s}$ , for large  $k$  and small  $\eta$ . Equation (3.11) suggests the balance  $\lambda \sim \eta k^2$  and  $\lambda \chi \sim \eta B$  so that at leading order

$$(\lambda + \eta k^2)\chi = -\frac{2\varepsilon\eta B}{h^2}, \quad (3.15)$$

$$(\lambda + \eta k^2)\frac{B}{h^2} = ik\chi\frac{1}{h}\frac{\partial}{\partial n}\left(\frac{v}{h^2}\right) \equiv v_1 ik\chi, \quad (3.16)$$

say, where  $v_1$  is constant on the fast  $s$ -scale  $1/k$ . These relations give the leading-order behaviour of  $\lambda$ :

$$\lambda = -\eta k^2 \pm (-2\varepsilon\eta v_1 ik)^{1/2} \implies \text{Re}[\lambda] = (\varepsilon v_1 \eta k)^{1/2} - \eta k^2, \quad (3.17)$$

choosing the root with the greater real part. Now as  $\eta \rightarrow 0$ , it is clear that  $\text{Re}[\lambda]$  is positive. Furthermore, it is easy to calculate the value of  $k$  for which this real part is maximum. This value scales as  $k \sim \eta^{-1/3}$  as  $\eta \rightarrow 0$  giving

$$\text{Re}[\lambda] = (\varepsilon^2 a_1^2 \eta)^{1/3} [4^{-1/3} - 16^{-2/3}] + O(\eta^{5/9}). \quad (3.18)$$

It should be noted that this is a local structure, and that  $a_1$  varies slowly over the boundary. For the square cross-section used here,  $a_1$  is maximum towards the inner boundary. For the flow of figure 7, equation (3.18) predicts  $\text{Re}[\lambda] \sim 0.545 R_m^{-1/3}$  as shown on figure 8. The presence of  $\varepsilon$  in (3.18) indicates that it is peculiar to helical symmetry. Note that it vanishes as  $\varepsilon \rightarrow \infty$  as  $\varepsilon a_1 \rightarrow 0$  in that limit (Zabielski & Mestel 1998a).

The above calculation ignores the boundary conditions, as the  $n$ -derivatives do not appear at leading order. A more precise analysis for a general cross-section  $S$ , deriving the structure normal to the surface, is given in the Appendix. To summarize the results, kinematic dynamos usually exist for flow fields with only a down-pipe component, even those satisfying a no-slip condition with perfectly conducting walls. At high  $R_m$ , the growing modes vary on a small tangential scale and a slightly larger normal scale ( $\eta^{1/3}$  and  $\eta^{2/9}$  respectively). Adjustment to the surface boundary conditions occurs over a passive sublayer of thickness  $\eta^{1/3}$ .

### 3.3. No primary flow

For completeness, flows with  $v = 0$  are now considered briefly. Equations (2.16), and (2.17) become

$$\frac{\partial \chi}{\partial t} + \frac{1}{r} J(\Psi, \chi) = \eta \left( \mathcal{L} \chi - \frac{2\varepsilon}{h^2} B \right), \quad (3.19)$$

$$\frac{\partial B}{\partial t} + \frac{h^2}{r} J\left(\Psi, \frac{B}{h^2}\right) = \eta \mathcal{L} B + \frac{2\varepsilon}{h^2} \frac{\partial \chi}{\partial t}. \quad (3.20)$$

The important ‘differential rotation’ linkage term in (3.20) disappears in this case, and only the weaker  $\partial \chi / \partial t$  term remains. In the cylindrical geometry of Ruzmaikin *et al.* (1988), Gilbert (1988) and Bassom & Gilbert (1997), where the pipe is replaced by a

complete cylinder and  $\psi = \psi(r)$ , a dynamo may occur. Here, in a pipe with a no-slip boundary and perfectly conducting walls, no growing modes were found numerically. A kinematic flow with this structure was used as a simple test of the neutral mode analysis of §3.1.

It has been shown in this section that no helically symmetric dynamo results from pressure-driven flow in the square pipe with perfectly conducting walls unless the cross-pipe component is artificially weakened. Similar results are found when the exterior conductivity is finite, so that it is the geometry, rather than the electric boundary conditions, which inhibits the dynamo.

In the next section, flow in the tall pipe of figure 1 is considered. The cross-pipe stretching is weaker in that case and a dynamo is found for the full laminar pipe flow.

#### 4. Dynamo action with conducting exterior

In this section, the magnetic field is permitted to diffuse out of the pipe, as is likely to occur in practice. Firstly, the Ponomarenko (1973) dynamo is rederived and then it is shown that steady laminar pipe flow acts as a dynamo in this case.

##### 4.1. The Ponomarenko dynamo

As discussed in (3.13), for the well-known Ponomarenko dynamo, the velocity terms disappear in the helical formulation. For simplicity, it is usual to assume the same diffusivity  $\eta$  inside and outside the cylinder  $r=1$ . The solution to (2.16) and (2.17) then takes the form inside the cylinder, following Kelvin (1880)

$$\chi = (a_1 I_m(vr) + a_2 r I'_m(vr)) e^{im\phi} \quad \text{where} \quad v = \sqrt{\lambda/\eta + m^2 \varepsilon^2}. \quad (4.1)$$

A similar representation holds for  $B$ , while in  $r > 1$  the representation is  $\chi = a_3 K_m + a_4 r K'_m$ . The boundary conditions (2.24) then lead to four linear conditions on the constants  $a_i$ , in which the discontinuity in  $v$  at  $r=1$  is crucial. After some algebra, this reduces to

$$im\varepsilon(K_m(v)I'_m(v) + I_m(v)K'_m(v)) = \eta v. \quad (4.2)$$

Not surprisingly, this is in exact agreement with the result obtained using cylindrical coordinates, when a helically symmetric mode is sought, e.g. Gilbert (2003).

A test of the numerical code was conducted as follows. The velocity discontinuity across  $r=1$  is smoothed out over about 10 grid points and a perfectly conducting boundary is introduced at  $r=2$ , on which the conditions  $\chi=0$  and  $\partial B/\partial r=0$  are imposed. In the  $\phi$ -direction  $2\pi$ -periodicity is imposed. In figure 9 the fastest growing solution obtained is drawn when  $R_m=10^3$  and  $\varepsilon=1$ . The familiar Ponomarenko structure appears, with in this case a mode  $m=4$  and a growth rate  $\text{Re}(\lambda)=0.047$ . For the pure Ponomarenko problem with a velocity  $v(r)$  discontinuous at  $r=1$ ,  $m=4$  has  $\text{Re}(\lambda)=0.0475$  but the preferred mode has  $m=3$  and  $\text{Re}(\lambda)=0.0477$ , in keeping with (4.2). There is thus a small difference between the numerical and theoretical solutions. The boundary at  $r=2$  has minimal effect, as the field decays exponentially away from  $r=1$ . More significant is the distance  $\delta$  over which  $v(r)$  falls to zero. This alters the preferred mode when  $\delta \sim R_m^{-1/3}$ . For the case presented  $\delta=0.1$  and the growth rates are affected. As  $\delta$  is decreased, it is found that the theoretical values are approached.

##### 4.2. A laminar pressure-driven dynamo

In this section it is shown that the steady flow of conducting fluid in a helical pipe driven by a pressure difference can drive a dynamo. Three cases have been considered:

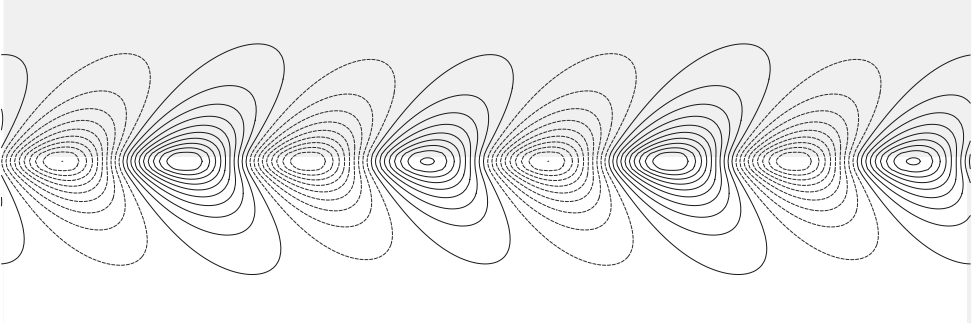


FIGURE 9. A Ponomarenko-like dynamo with a continuous velocity field for  $R_m = 10^3$ . The  $\mathbf{H}$ -component  $B$  is shown with the axis of the cylinder at the bottom. The real part of the growth rate is 0.047 and the fastest growing mode has  $m = 4$  as shown. For the discontinuous velocity field  $m = 3$  is maximal with a growth rate 0.0477 in accordance with (4.2), whereas  $m = 4$  has a growth rate of 0.0475.

Grid	$R_m = 15^3$	$R_m = 17^3$	$R_m = 20^3$
$120 \times 180$	0.00484632 + i0.0103017	0.00444049 + i0.00468306	0.00330619 + i0.00199776
$160 \times 240$	0.00477356 + i0.0101948	0.0043816 + i0.00463633	0.00327049 + i0.00197132
$240 \times 360$	0.00467345 + i0.0102098	0.0043424 + i0.00468166	0.00325175 + i0.00198048

TABLE 1. Table of growth rates for the tall pipe flow of figure 10 and the same conductivity inside and out.

when the conductivity of the exterior region is zero, infinite or the same as in the interior. Only the latter case is presented here.

Equations (2.16) and (2.17) are now solved in both  $V$  and  $\widehat{V}$ , with zero velocity in  $\widehat{V}$ . The exterior domain is rendered finite by introducing a perfectly conducting surface at  $r = r_{max}$  on which  $\chi = 0$  and  $\partial B / \partial r = 0$ . In the results presented here,  $r_{max} = 2$ . The field decays exponentially in the exterior and is not very sensitive to the value of  $r_{max}$ .

The appropriate conditions on the axis  $r = 0$  are  $\partial B / \partial r = 0$  and  $\partial \chi / \partial r = 0$ . In the  $\phi$ -direction  $2\pi$ -periodicity is imposed. The exterior grid was uniform in the  $r$ -direction, but stretched smoothly in the  $\phi$ -direction to provide greater resolution in the areas of interest.

In figure 11 the fastest growing eigenfunction is drawn for  $R_m = 20^3$ . For the sake of compactness, only a portion of the external region is shown in the periodic  $\phi$ -direction. Comparison with figure 10 illustrates the importance of field stretching along the separatrix of the cross-pipe motion as  $R_m$  increases. The active dynamo resides in the region of weak cross-pipe flow. In figure 12, the variation of the real and imaginary parts of the corresponding growth rate is drawn. Growth occurs for  $R_m \geq 12^3$  and is maximal for  $R_m \simeq 15^3$ . As  $R_m \rightarrow \infty$ , it appears that  $\lambda \sim R_m^{-1/3}$ .

Special attention was given to a few cases to determine the robustness of the results to variations in the spatial and temporal step lengths. The structure of the eigenfunction varies relatively little, but it is much harder to obtain the complex eigenvalue accurately. For a fixed spatial grid, the time step was decreased to a level where the eigenvalue as calculated from an average over several cycles did not change. As the grid size is decreased, the convergence of the imaginary part of the eigenvalue is non-monotonic. Typical variation of  $\lambda$  with grid size is shown in table 1.

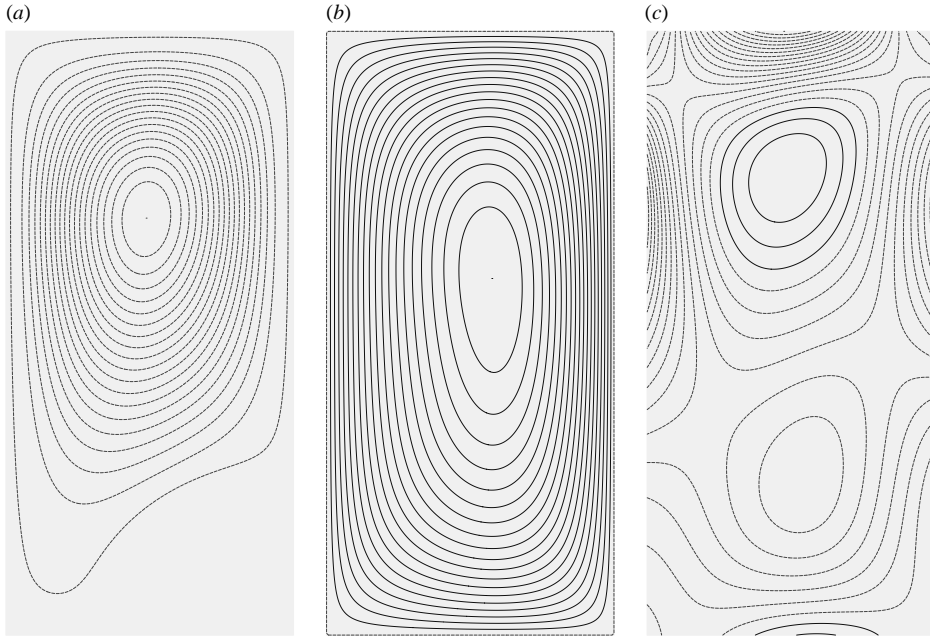


FIGURE 10. Flow in tall pipe for  $R_e = 10^3 h_b$ : (a)  $\Psi$ ; (b)  $v$ ; (c)  $\xi$ . The second  $\psi$ -gyre is very weak, permitting dynamo action.

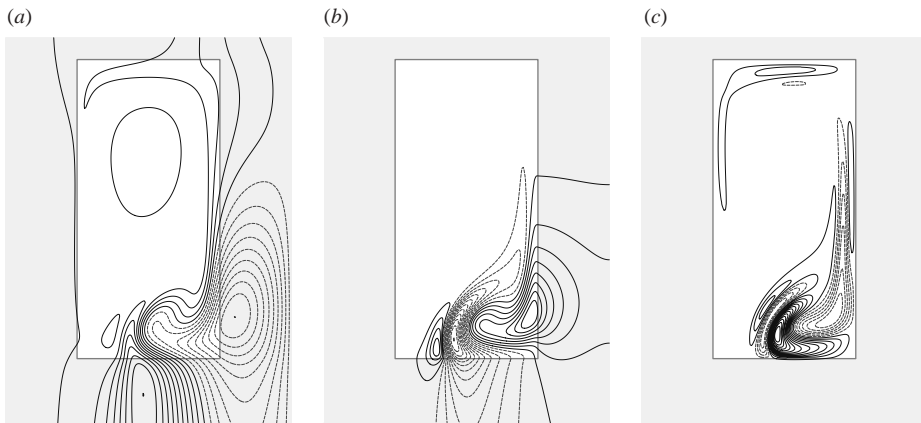


FIGURE 11. Fastest growing mode for  $R_m = 20^3$  and flow as in figure 10: (a)  $\chi$ ; (b)  $B$ ; (c)  $\gamma$ . Same conductivity inside and out. Only part of the external domain is shown.

The results in figures 11 and 12 use a  $240 \times 360$  grid over the entire computational domain. The real and imaginary parts of  $\lambda$  are found to be of similar magnitude, although when perfectly conducting walls are used the imaginary part is very small, perhaps zero. The time-evolutionary method is not the most efficient for calculating eigenvalues, but was chosen with a view to future extension into the nonlinear regime.

Although it is not easy to obtain the growth rates to high accuracy, it is certain that dynamo action can occur for helically symmetric steady pipe flow. Whether or not such action occurs seems to be determined by the pipe shape, rather than by the magnetic boundary conditions, which affect more the critical value of  $R_m$ .

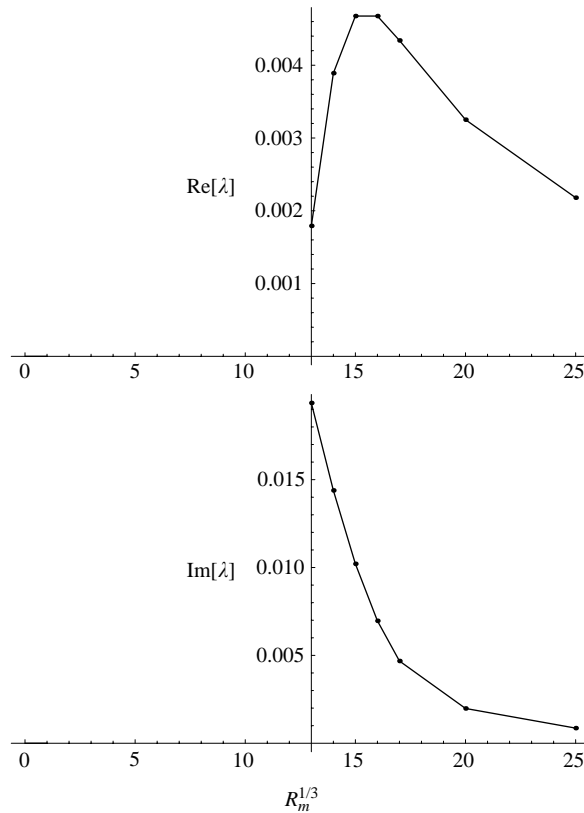


FIGURE 12. The behaviour of  $\lambda(R_m)$  for the tall pipe with  $R_e = 10^3 h_b$  and the same external conductivity.

The mechanism seems to be as follows: ‘poloidal’ field,  $\chi$ , is wound round by gradients in the ‘toroidal’ velocity  $v$  to generate toroidal field,  $B$ . The helical symmetry ensures that  $\eta B$  can act as a source term for  $\chi$ . Simultaneously, both  $\chi$  and  $B$  are stretched in the  $(r, \phi)$ -plane by the poloidal velocity  $\Psi$ , to a level where they can be dissipated. For the square pipe, the cross-pipe flow obliterates the dynamo. However, for the tall pipe, the field can grow in the weaker of the two circulatory regions of the secondary motion. A dynamo is also observed in this case for perfectly conducting walls (Zabielski & Mestel 2004) and for very weakly conducting exterior.

The nonlinear saturation of these dynamo modes is currently under investigation and the results will be presented in a future paper.

## 5. Concluding remarks

It has been shown that the three-dimensional nature of steady helically symmetric solutions to the steady Navier–Stokes equations can drive a dynamo without recourse to a turbulent  $\alpha$ -effect or similar. This is the first steady pressure-driven dynamo to be found. The critical  $R_m \sim 1000$  but it should not be forgotten that  $R_m$  was defined with respect to the maximum down-pipe velocity, so that the effective  $R_m$  is arguably smaller. This may be still more significant for structures where the growth occurs close to the pipe boundary, and the local  $v$  is noticeably smaller.

This paper has only considered steady laminar flow, though in practice a laboratory dynamo would almost certainly be turbulent. The mean velocity profiles for turbulent flow would differ from those considered above, but should also drive dynamos. Calculations were performed for potential flow, which is a very simple model of mean turbulent flow, and dynamo growth was obtained. However it is not clear how nonlinear saturation should be included in this case.

Dynamo action has been found only in cases where the cross-pipe flow is weak. The stagnation point structure, where the growing modes exhibit strong stretching along the separatrix, has a critical effect. It has been argued that a somewhat ideal laminar flow at extremely high  $R_e$  may drive a dynamo even in the square pipe case, but moderate  $R_e$  suffices for the tall pipe. The dynamo action appears also to be opposed, but not prevented, by perfectly conducting walls.

Only those modes with the same helical symmetry as the flow have been considered. It is thus conceivable that dynamo instability might occur for some flows which have been found stable in this paper; clearly, however, some dynamo action will occur when predicted here, even should a non-symmetric mode have slightly higher growth rate.

The results are relevant to the construction of laboratory dynamos. In the Riga dynamo the external medium is stationary liquid metal which motivated the choice of external conductivity in §4.2. Dynamo action for the tall pipe is also found for insulating, very weakly conducting and perfectly conducting exteriors. The dynamos found in this paper can be extended into the nonlinear regime and this work is in progress.

This collaborative work was supported by the EPSRC grant GR/R71191. Dr Zabielski is grateful to the Mathematics department of Imperial College for its hospitality.

### Appendix. Eigenfunction asymptotics when $\psi = 0$ as in §3.2

In this appendix, the structure of the growing mode with  $\psi = 0$  is investigated in the limit  $\eta \rightarrow 0$ . Near the surface  $S$ , with normal and tangential coordinates  $(n, s)$ , solutions are sought  $\propto e^{\lambda t + iks}$  with  $k \sim \eta^{-1/3}$  and  $\lambda \sim \eta^{1/3}$ . For a small scale  $\delta$  to be determined but with  $k\delta \gg 1$ , define  $y = n/\delta$  and expand

$$\lambda = \eta^{1/3}(\lambda_0 + \delta\lambda_1 + O(\delta^2)), \quad \frac{1}{h} \frac{\partial}{\partial n} \left( \frac{v}{h^2} \right) = v_1 + \delta v_2 y + O(\delta^2) \quad (\text{A } 1)$$

where the  $v_i$  vary with  $s$  on an  $O(1)$  scale. The operator  $\mathcal{L}$  then locally takes the form

$$\mathcal{L}\chi = \frac{\chi_{yy}}{\delta^2} - k^2(1 + c\delta y)\chi + O(k, 1/\delta)$$

where  $c(s)$  is determined by the local geometry. On a wall with  $\phi$  constant  $c = 0$ . Writing  $\widehat{B} = B/h^2$  and noting that  $\mathcal{L}(B/h^2) = (1/h^2)\mathcal{L}(B) + O(k)$ , (3.11) and (3.12) become to first order

$$(\lambda + \eta k^2)\chi + 2\varepsilon\eta\widehat{B} = \frac{\eta}{\delta^2}\chi_{yy} - (ck^2\eta\delta)y\chi, \quad (\text{A } 2)$$

$$(\lambda + \eta k^2)\widehat{B} - v_1 ik\chi = \frac{\eta}{\delta^2}\widehat{B}_{yy} - (ck^2\eta\delta)y\widehat{B} + v_2 ik\delta y\chi. \quad (\text{A } 3)$$

For flows not satisfying a no-slip condition, there would be an additional term  $v_s\chi_n$  from the Jacobian in (A 3) and the structure would be different.

Taking  $k = \kappa\eta^{-1/3}$ , where  $\kappa = O(1)$ , the terms on the right-hand side of (A 2) and (A 3) are of the same order when

$$\delta = \eta^{2/9}.$$

Thus introducing the vector  $\mathbf{x} = (\chi, \eta^{2/3} \widehat{B})^T$ , (A 2) and (A 3) take the form

$$\mathbf{A}\mathbf{x} + \lambda_0 \mathbf{x} = \delta[\mathbf{x}_{yy} - y \mathbf{C}\mathbf{x} - \lambda_1 \mathbf{x}] \quad (\text{A } 4)$$

where

$$\mathbf{A} = \begin{pmatrix} \kappa^2 & 2\varepsilon \\ -i\kappa a_1 & \kappa^2 \end{pmatrix} \quad \text{and} \quad \mathbf{C} = \begin{pmatrix} -c\kappa^2 & 0 \\ i\kappa a_2 & -c\kappa^2 \end{pmatrix}. \quad (\text{A } 5)$$

In the singular limit  $\delta \rightarrow 0$ , this equation reduces to (3.15) and (3.16), with solution

$$\mathbf{x} = g(y)\mathbf{x}_0 + O(\delta) \quad (\text{A } 6)$$

where  $\mathbf{x}_0$  is the constant eigenvector of  $\mathbf{A}$  corresponding to  $\lambda_0$ . The amplitude  $g(y)$  is determined at next order in  $\delta$ , by imposing orthogonality with the solution to the adjoint problem (the Fredholm alternative).

Defining the eigenvectors  $\mathbf{A}\mathbf{x}_0 = -\lambda_0 \mathbf{x}_0$  and  $\overline{\mathbf{A}}^T \mathbf{w}_0 = -\overline{\lambda_0} \mathbf{w}_0$  where the overbar denotes a complex conjugate, then in (A 4)  $\mathbf{x}$  has a solution at order  $\delta$  only if

$$g'' - \beta y g - \lambda_1 g = 0 \quad \text{where} \quad \beta = \frac{\overline{\mathbf{w}_0}^T \mathbf{C} \mathbf{x}_0}{\overline{\mathbf{w}_0}^T \mathbf{x}_0}. \quad (\text{A } 7)$$

One boundary condition on  $g$  derives from  $\mathbf{x} \rightarrow 0$  as  $y \rightarrow \infty$ . At the fluid surface  $S$  an appropriate version of (2.26) should be applied. However, when  $\eta = 0$ , it follows from (A 6) that  $\chi \propto B$ , and the conditions  $\chi = 0$  and  $B_y = 0$  cannot be applied simultaneously to (A 4). A lower layer is necessary in this case, in which  $n \sim s \sim \eta^{1/3}$ . Writing  $n = \eta^{1/3} Y$ , in this lower layer to leading order

$$\mathbf{x}_{YY} = \mathbf{A}\mathbf{x} + \lambda_0 \mathbf{x},$$

whose solution with appropriate behaviour as  $Y \rightarrow \infty$  takes the form

$$\mathbf{x} = (d_1 + d_2 Y)\mathbf{x}_0 + d_3 e^{-\mu Y} \tilde{\mathbf{x}}$$

for constants  $d_i$ , where  $\tilde{\mathbf{x}}$  is the other eigenvector of  $\mathbf{A}$  and  $\mu$  has a positive real part. It is possible to satisfy the conditions  $\chi = 0$  and  $B_Y = 0$  on  $Y = 0$  only if  $d_2 \neq 0$ . This implies  $\mathbf{x} \sim Y$  as  $Y \rightarrow \infty$  and matching with the upper layer then requires  $\mathbf{x} \sim y$  as  $y \rightarrow 0$ , so that  $g(0) = 0$  in (A 6).

The appropriate boundary conditions on the outer layer (A 7) to match with the core and the lower layer are thus

$$g(0) = 0 \quad \text{and} \quad g \rightarrow 0 \quad \text{as} \quad y \rightarrow \infty. \quad (\text{A } 8)$$

The Airy equation (A 7) with (A 8) fixes the eigenvalue perturbation  $\lambda_1$  and the leading-order amplitude  $g(y)$ . The solution is

$$g(y) = \text{Ai}[\beta^{1/3} y + \lambda_1 \beta^{-2/3}].$$

The zeros of the Airy function occur on the real axis, which determines the phase relation between  $\beta$  and  $\lambda_1$ . This demonstrates the consistency of the arguments in § 3.2.

#### REFERENCES

- BASSOM, A. P. & GILBERT, A. D. 1997 Nonlinear equilibration of a dynamo in a smooth helical flow. *J. Fluid Mech.* **343**, 375–406.  
 BATCHELOR, G. K. 1956 On steady laminar flow with closed streamlines. *J. Fluid Mech.* **1**, 177–190.

- BENTON, E. R. 1979*a* Kinematic dynamo action with helical symmetry in an unbounded fluid conductor. Part I. *Geophys. Astrophys. Fluid Dyn.* **12**, 313–344.
- BENTON, E. R. 1979*b* Kinematic dynamo action with helical symmetry in an unbounded fluid conductor. Part II. *Geophys. Astrophys. Fluid Dyn.* **12**, 345–358.
- BRUMMELL, N. H., CATTANEO, F. & TOBIAS, S. M. 1998 Linear and nonlinear dynamo action. *Phys. Lett. A* **249**, 437–442.
- CHILDRESS, S. & GILBERT, A. D. 1995 *Stretch, Twist, Fold: the Fast Dynamo*. Springer.
- CHILDRESS, S., LANDMAN, M. & STRAUSS, H. 1989 Steady motion with helical symmetry at large Reynolds number. In *Proc. IUTAM Symp. on Topological Fluid Dynamics* (ed. H. K. Moffatt & A. Tsinober) pp. 216–224. Cambridge University Press.
- DOBLER, W., FRICK, P. & STEPANOV, R. 2003 Screw dynamo in a time-dependent pipe flow. *Phys. Rev. E* **67**, 1–10.
- DRITSCHEL, D. 1991 Generalised helical Beltrami flows in hydrodynamics and magnetohydrodynamics. *J. Fluid Mech.* **222**, 525–541.
- ELTAYEB, I. A. & LOPER, D. E. 1988 On steady kinematic helical dynamos. *Geophys. Astrophys. Fluid Dyn.* **44**, 259–269.
- FAUVE, S. 2004 Dynamo experiments. Newton Institute Program MHD of Stellar Interiors <http://www.newton.cam.ac.uk/webseminars/pg+ws/2004/msiw01/0916/fauve1>.
- GAILITIS, A. & FREIBERG, YA. 1977 Theory of a helical MHD dynamo. *Magnetohydrodynamics* **12**, 127–130.
- GAILITIS, A. & FREIBERG, YA. 1980 Nonuniform model of a helical dynamo. *Magnetohydrodynamics* **16**, 11–15.
- GILBERT, A. D. 1988 Fast dynamo action in the Ponomarenko dynamo. *Geophys. Astrophys. Fluid Dyn.* **44**, 241–258.
- GILBERT, A. D. 2003 Dynamo theory. In *Handbook of Mathematical Fluid Dynamics, Vol. 2* (ed. S. Friedlander & D. Serre), pp. 355–441. Elsevier.
- KELVIN, LORD 1880 Vibrations of a columnar vortex. *Phil. Mag.* **10**, 155–168.
- KIM, E. J., HUGHES, D. W. & SOWARD, A. M. 1999 An investigation into high conductivity dynamo action driven by rotating convection. *Geophys. Astrophys. Fluid Dyn.* **91**, 303–332.
- LANDMAN, M. 1990 Time dependent helical waves in rotating pipe flow. *J. Fluid Mech.* **221**, 289–310.
- LORTZ, D. 1968 Exact solutions of the hydrodynamic dynamo problem. *Plasma Phys.* **10**, 967–972.
- MATTHEWS, P. C. 1999 Dynamo action in simple convective flows. *Proc. R. Soc. Lond. A* **455**, 1829–1840.
- PLUNIAN, F., MARTY, P. & ALEMANY, A. 1999 Kinematic dynamo action in a network of screw motions: application to the core of a fast breeder reactor. *J. Fluid Mech.* **384**, 137–154.
- PONOMARENKO, Y. B. 1973 On the theory of hydromagnetic dynamos. *Zh. Prikl. Mekh. Tekh. Fiz.* **6**, 47–51.
- RÄDLER, K.-H. & CĒBERS, A. 2002 The special issue: MHD dynamo experiments. *Magnetohydrodynamics* **38**.
- ROBERTS, G. O. 1972 Dynamo action of fluid motions with two-dimensional periodicity. *Phil. Trans. R. Soc. Lond. A* **271**, 411–454.
- ROBERTS, P. H. & SOWARD, A. M. 1992 Dynamo theory. *Annu. Rev. Fluid Mech.* **24**, 459–512.
- RUZMAIKIN, A. A., SOKOLOFF, D. D. & SHUKUROV, A. 1988 Hydromagnetic screw dynamo. *J. Fluid Mech.* **197**, 39–56.
- WILLIS, A. P. & BARENGHI, C. F. 2002 A Taylor-Couette dynamo. *Astr. Astrophys.* **393**, 339–343.
- ZABIELSKI, L. & MESTEL, A. J. 1998*a* Steady flow in a helically symmetric pipe. *J. Fluid Mech.* **370**, 297–320.
- ZABIELSKI, L. & MESTEL, A. J. 1998*b* Unsteady blood flow in a helically symmetric pipe. *J. Fluid Mech.* **370**, 321–345.
- ZABIELSKI, L. & MESTEL, A. J. 2004 Dynamo action in steady helical pipe flow. In *Proc. XXI ICTAM Symposium, Warsaw 2004*. Kluwer.